Marcus Bell-Shaped Electron Transfer Kinetics Observed in an Arrhenius Plot

Morteza M. Waskasi, Gerdenis Kodis, Ana L. Moore, Thomas A. Moore, Devens Gust[†] and Dmitry V. Matyushov [*,‡]

†*School of Molecular Sciences, Arizona State University, PO Box 871604, Tempe, AZ 85287-1604*

‡*Department of Physics and School of Molecular Sciences, Arizona State University, PO Box 871504, Tempe, AZ 85287-1504*

E-mail: dmitrym@asu.edu

Abstract

The Marcus theory of electron transfer predicts a bell-shaped dependence of the reaction rate on the reaction free energy. The top of the "inverted parabola" corresponds to zero activation barrier when the electron-transfer reorganization energy and the reaction free energy add up to zero. Although this point has traditionally been reached by altering the chemical structures of donors and acceptors, the theory suggests that it can also be reached by varying other parameters of the system including temperature. We find here dramatic evidence of this phenomenon from experiments on a fullerene-porphyrin dyad. Following photoinduced electron transfer, the rate of charge recombination shows a bell-shaped dependence on the inverse temperature, first increasing with cooling and then decreasing at still lower temperatures. This non-Arrhenius rate law is a result of a strong, approximately hyperbolic, temperature variation of the reorganization energy and the reaction free energy. Our results provide potentially the cleanest confirmation of the Marcus energy gap law so far since no modification of the chemical structure is involved.

Keywords: Marcus energy gap law, electron transfer, non-Arrhenius rate law, reorganization energy, fullerene dyad, entropy of activation

Introduction

The Marcus theory of electron transfer reactions marked the arrival of modern 20th century science to chemical reaction kinetics. It predicted a result that first seemed odd and utterly counter-intuitive (a situation similar to the advent of quantum mechanics): the bell-shaped dependence of the reaction rate on the reaction free energy.[1,2] The theory suggested that the reaction rate should first increase when lowering the standard reaction free energy ΔG_0 (increasing the driving force $-\Delta G_0$), which was consistent with the empirical evidence of the time, but then should start decreasing after passing through a maximum. At the time when this second branch of the energy-gap law, dubbed the inverted region, was suggested, it was not known experimentally and contradicted linear free-energy relationships empirically established in physical organic chemistry. It took several decades of scrutiny and final experimental breakthrough by Miller and Closs[3,4] to prove the prediction. The current textbook energy gap law of electron transfer reactions is the inverted parabola combining the normal region at $-\Delta G_0 < \lambda$ ("N" in Figure 1a) with the inverted region at $-\Delta G_0 > \lambda$ ("I" in Figure 1a); λ is the Marcus reorganization energy of electron transfer. The top of the inverted parabola marks zero activation barrier satisfying the condition[5]

$$\lambda + \Delta G_0 = 0 \tag{1}$$

The bell-shaped energy gap law has been confirmed for a number of donor-acceptor complexes.[6–8] Non-molecular systems, such as quantum dots and nanoparticles,[9] have been tried, but the inverted region could not been observed.[10] Most tests of the Marcus model attempted so far have followed the strategy originally suggested by Miller and co-workers[3,4] to alter the chemical structure of the donor and acceptor. Alternative approaches varied the donor-acceptor distance[11,12] to change the reorganization energy or applied an external electric field[13] to cross the point of activationless electron transfer. Here we report a potentially cleanest approach to testing the bell-shaped energy gap law achieved by varying temperature. The fundamental basis of this new phenomenology is a strong, inverse with temperature, variation of the reorganization energy.

The Arrhenius law

$$k_{\mathrm{ET}} \propto \exp\left[-G_a(T)/(k_{\mathrm{B}}T)\right] \tag{2}$$

is another iconic result of chemical kinetics. The law, when applied to the rate constant of electron transfer k_{ET}, implies the decrease of the rate with cooling and a linear relation be-

tween the logarithm of the reaction rate $\ln(k_{\rm ET})$ and the inverse temperature $1/T$. Deviations from strict linearity have been observed in extended temperature ranges. For glass-forming materials, the activation free energy $G_a(T)$ increases with lowering temperature for a number of relaxation phenomena.[14] However, the generally accepted qualitative result is that cooling should lower the rate of a chemical reaction or the rate of relaxing the external stress (relaxation rate).

Here we propose that the "counter-intuitive" bell-shaped Marcus law can be extended into the domain of temperature as the rate altering parameter to produce a bell-shaped dependence of the rate vs the inverse temperature (Arrhenius coordinates, Figure 1b). In this scenario, the rate first increases with cooling, opposite to the prediction of the Arrhenius law, reaches the maximum of no barrier, and then starts to drop with further cooling, in qualitative agreement with the Arrhenius law.

This situation is expected to occur for electron-transfer reactions positioned in the Marcus inverted region at high temperatures. If the sum $\lambda + \Delta G_0$ passes through zero with decreasing temperature, one arrives at the condition of activationless electron transfer at some intermediate temperature T^* (eq (1)) to cross to the normal region of electron transfer at lower temperatures (Figure 1b).

It is clear that in order to realize this scenario in a typically narrow range of temperatures accessible to experiments, both λ and ΔG_0 have to significantly change with temperature. The temperature variation of the reorganization energy and the driving force was not a significant issue in the original Marcus formulation.[1,2] The theory estimated the reorganization energy based on dielectric continuum adopted to model the solvent. The relations following from such models, going back to the Born formula for the free energy of ion solvation,[15] do not anticipate a significant variation of either λ or ΔG_0 with temperature. This expectation is basically consistent with observations for reactions in solid materials, which can be reasonably represented by dielectric models.

Liquid solvents, in contrast to continuum dielectrics, possess a broad range of fluctuating degrees of freedom wherein structural fluctuations occur. This lack of rigidity, incorrectly modeled by dielectric continuum, makes the Born equation and all results based on it poor predictors of the solvation entropy.[16–18]

Dipole rotations and dipole translations are two major collective modes of polar liquids contributing to the fluctuations of the donor-acceptor energy gap used as the reaction coordinate in modern theories of electron transfer.[19–21] It was found that these two modes of thermal agitation lead to distinctly different temperature laws when combined in the calculation of the reorganization energy: approximately constant for dipolar rotations and inversely proportional to temperature for dipolar translations (density fluctuations).[22] The overall dependence of the reorganization energy on temperature is hyperbolic, $\lambda = \lambda_p + \sigma_d^2/(2k_{\rm B}T)$, at constant-volume conditions (σ_d^2 is the Gaussian variance of the energy gap produced by density fluctuations and λ_p is the reorganization energy caused by dipolar reorientations).[23] The typical experimental constant-pressure conditions add thermal expansivity of the solvent, but preserve the general phenomenology (Figure 2).

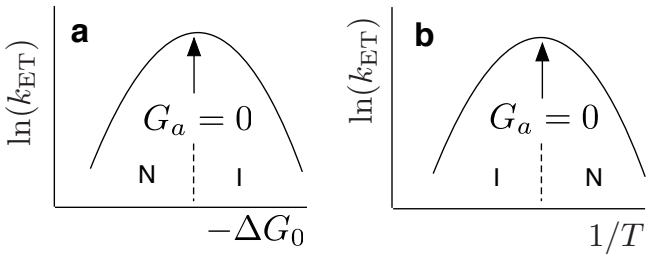

Figure 1: The bell-shaped (Marcus) energy gap law vs the reaction driving force $-\Delta G_0$ (a) and the bell-shaped law vs $1/T$ (Arrhenius coordinates, b). In both cases, the top of the inverted parabola corresponds to zero activation free energy, $G_a = 0$. "N" and "I" indicate, correspondingly, the normal and inverted regions of electron transfer

Experimental testing of the theory has supported the decrease of the reorganization energy with increasing temperature.[18,24,25] Computer simulations are also consistent with this

basic physical picture.[26] A similar, but less pronounced trend is observed for the reaction free energy ΔG_0 (Figure 2).

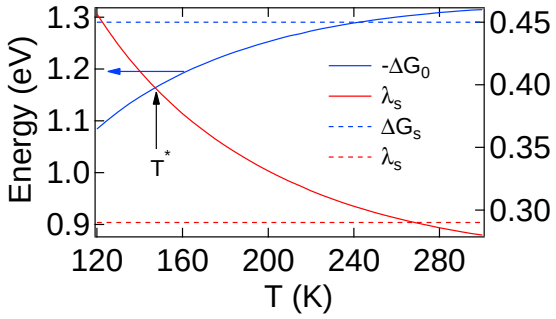

Figure 2: Temperature variation of the solvent reorganization energy $\lambda_s(T)$ (red solid line) and the driving force $-\Delta G_0$ (black solid line) calculated for the charge recombination reaction in 2-methyltetrahydrofuran (MTFH). The left axis refers to the results of the microscopic solvation model SolvMol,[27,28] while the right axis and the dashed lines refer to λ_s (red) and ΔG_s (blue) calculated in the dielectric continuum model of the solvent by using the software package DelPhi.[29] The vertical arrow indicates the temperature T^* at which zero activation barrier, $G_a = 0$, is reached in the SolvMol calculations (eq (1) and Figure 1)

The strong temperature decay of λ with increasing temperature can be combined with the corresponding increase of the driving force to reach the point of no barrier when they cross, $\lambda(T^*) = -\Delta G_0(T^*)$ (vertical arrow in Figure 2). This is the point of the top of the inverted Marcus parabola in the Arrhenius coordinates predicted theoretically.[22] There was an early experimental indication of such a behavior from Heitele *et al.*[30] However, the rates were measured in a relatively narrow range of temperatures and it was not clear if the observed effect is just an artifact of nearly activationless kinetics. Here, with the use of 2-methyltetrahydrofuran (MTHF) as the solvent, we have considerably extended the range of accessible temperatures and were able to demonstrate the robustness of the bell-shaped kinetic temperature law.

Our new experimental results and calculations support the view that the bell-shaped Arrhenius law is caused by the temperature dependence of solvation free energies entering the activation barrier. The experimental data were obtained for the reaction of intramolecular charge recombination in the donor-acceptor dyad composed of porphyrin (P, donor) and fullerene (C_{60}, acceptor) moieties connected by a bridge (Figure 3). Charge recombination follows the formation of a charge-separated state $P^{\cdot+} - C_{60}^{\cdot-}$ by photoinduced electron transfer. This dyad, and an entire family of related donor-acceptor molecules, were among the first reported in the literature to produce long-lived photoexcited charge separated states down to temperatures close to 0 K. This property permits study of electron transfer over a relatively large temperature range.[31,32] Such molecules have attracted significant interest as potential building blocks of solar conversion devices.[32–35]

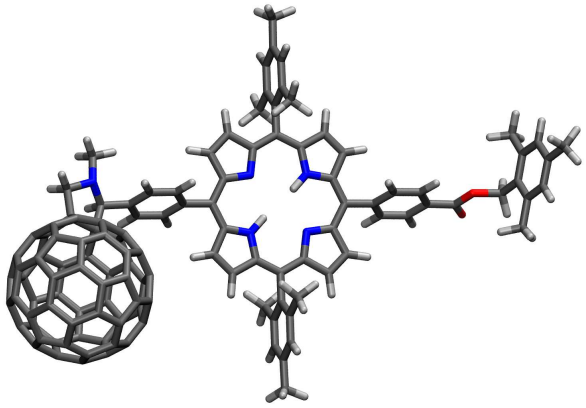

Figure 3: Structure of the porphyrin-fullerene dyad

A bell-shaped reaction kinetics in Arrhenius coordinates was previously reported by Kim *et al*[36] and later by Wasielewski and co-workers.[37] The complex kinetics was responsible for the observation in the first case. Further, conformational flexibility (torsional rotation), altering the probability of electron tunneling between the donor and acceptor, was suggested as the cause of the effect in the study by Wasielewski and co-workers.[37] In contrast, the dyad used in this study is relatively rigid conformationally such that no significant alteration of the donor-acceptor distance and of the tunneling probability is expected. This design eliminates con-

formational mobility as the cause of the non-Arrhenius temperature law.

Results

Our main focus here is on the charge recombination reaction, following the photoinduced creation of the charge separated porphyrin-fullerene biradical $P^{\cdot+} - C_{60}^{\cdot-}$ (Figure 3)

$$P^{\cdot+} - C_{60}^{\cdot-} \xrightarrow{k_R} P - C_{60} \qquad (3)$$

In this reaction scheme, the final state of electron transfer ($i = 2$) is the ground state of the dyad $P - C_{60}$. The initial state is the charge-separated complex $P^{\cdot+} - C_{60}^{\cdot-}$ ($i = 1$). The reaction rate constant is that of recombination, k_R, and the reaction free energy $\Delta G_0 = G_{02} - G_{01}$ is negative for charge recombination to the ground state (see Supplementary Figure S1 for the energy surfaces in the gas phase).

In addition to the charge recombination reaction, which shows the bell-shaped curve in the Arrhenius coordinates (Figure 4a), we consider two rates of charge separation (CS) from a photoexcited state produced either at porphyrin or at C_{60}. Although most of the excitation light was absorbed by the porphyrin in these experiments, the fullerene excited state is populated by singlet-singlet energy transfer, and can then undergo charge separation

$$\begin{aligned} P^* - C_{60} &\xrightarrow{k_{CS1}} P^{\cdot+} - C_{60}^{\cdot-} \\ P - C_{60}^* &\xrightarrow{k_{CS2}} P^{\cdot+} - C_{60}^{\cdot-} \end{aligned} \qquad (4)$$

Charge recombination and charge separation were studied experimentally and theoretically as a means of testing the consistency of the parameters obtained from analyzing these two kinds of electron transfer reactions.

The results of rate measurements vs temperature in MTHF solvent are shown by points in Figure 4. The experimental data clearly display a bell-shaped reaction law for charge recombination (Figure 4a), with the maximum indicating the activationless recombination reaction (eq (1)). For the photoinduced charge separation reactions, occurring in the Marcus normal region, no inverted region is present (Figure 4b). The details of the measurements and kinetic fitting are briefly summarized in Methods below and are given in more detail in the Supplementary Information (SI).

The main question raised by experimental evidence is what are the properties of λ and ΔG_0 required to obtain the bell-shaped law in the Arrhenius coordinates. Neither λ nor ΔG_0 are accessible from direct experimental measurements. An estimate of ΔG_0 is available from redox potentials, but such results apply to separate donors and acceptors reacting at an electrode in a medium containing ions, and are not very reliable when used for a donor-acceptor complex. One therefore has to resort to calculations to establish these parameters separately. The maximum in the Arrhenius coordinates puts a significant restriction on their values by imposing the condition of zero activation barrier at T^*. In addition, the complex shape of the Arrhenius plots significantly restricts the ability of standard models to reproduce the data without taking into account the temperature dependence of the activation free energy $G_a(T)$ in eq (2). Additional restrictions are imposed by the charge-separation rates (Figure 4b), which are reproduced here, together with the charge-recombination kinetics, using a single set of parameters (see below). Overall, these kinetic measurements provide us with a critical test of the theory's ability to calculate the activation barrier of an electron-transfer reaction in an extended range of temperatures.

The main physical reason for the curved shape of the Arrhenius plots shown in Figure 4a is a substantial variation of the solvent part of the activation barrier with temperature. It is given by the solvent reorganization energy λ_s and the solvent part of the reaction free energy ΔG_s. For organic systems there is typically a negligible contribution of internal vibrations to the classical reorganization energy, which is assumed here to originate entirely from the solvent, $\lambda = \lambda_s$. However, the internal reorganization energy λ_v associated with quantum vibrations is significant (Table 1 and discussion below). Further, the reaction free energy can be

separated into the energy gap in the gas phase ΔE_g (negative of the 0-0 transition energy between the ground and charge-separated states) and the free energy of solvation ΔG_s [38]

$$\Delta G_0 = \Delta E_g + \Delta G_s \tag{5}$$

The gas-phase component ΔE_g is in principle available from gas-phase quantum calculations, but the accuracy of those is not sufficient for the modeling of the kinetics (see SI). It is, therefore, extracted from fitting the experimental kinetic curves (Table 1). The solvation component requires solvation calculations, which are the main focus of the theoretical modeling. We show below that microscopic models of solvation are required to adequately account for the temperature variations of $\lambda_s(T)$ and $\Delta G_s(T)$.

The electron at the donor or acceptor interacts with the solvent by a number of interaction potentials. They are all electrostatic in origin, but are calculated from different multipoles (electrostatic charge, dipole moment, etc) and in different orders of the quantum-mechanical perturbation theory.[39] The most important among them for reactions in polar solvents is the interaction of the electron charge (monopole) with the solvent permanent dipoles, as assumed in the Marcus theory.[1] For weakly polar solvents, interactions of the electron with higher solvent multipoles gain in importance.[40–42] Interactions arising from the second-order quantum-mechanical perturbation theory include induction and dispersion forces. Fluctuations of these interaction potentials, producing corresponding fluctuations of the donor-acceptor energy gap, are caused by molecular translations.[43] The contribution of these interaction potentials to the activation barrier of electron transfer has been estimated and proved out to be small for reactions in MTHF (Figure S3 in SI). We therefore focus here on the dipolar component of the solvent effect.

Calculations of the effect of temperature on the solvation free energy and the solvent reorganization energy require accounting for the molecular nature of the solvent.[22,23,26] A possible avenue of exploring the solvent effect is

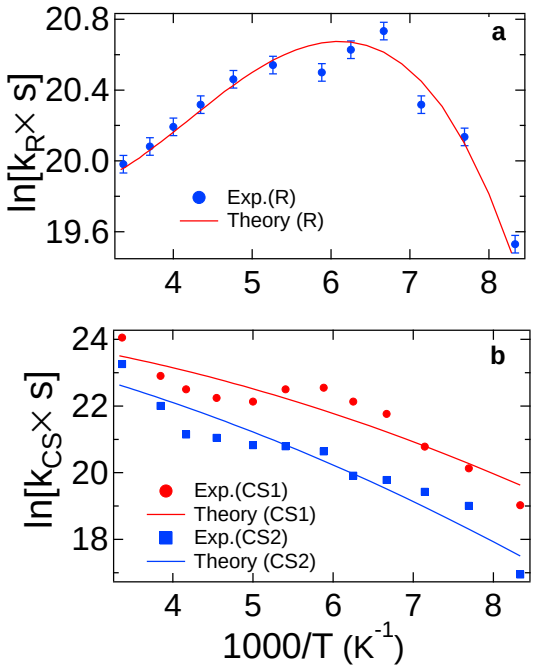

Figure 4: Rate constant in Arrhenius coordinates for charge recombination ($k_R(T)$, a) and charge separation ($k_{CS1}(T)$ and $k_{CS2}(T)$, b) in MTHF. The points represent experimental data and the solid lines refer to the theoretical calculations with the SolvMol package.[27,28] The experimental errors for CR in (a) are within 5% and for CS in (b) within 10%. The error bars in (b) are not shown since they are nearly the size of the points. All theoretical calculations were done with a single set of parameters listed in Table 1 (fitting parameters V and ΔE_g and calculated λ_v; experimental parameters of the solvent are used for the solvation calculations)

to use atomistic computer simulations, which provide, in principle, complete sampling of the solvent configurations not far from equilibrium. This approach is not a viable option for our purpose because a significant portion of the temperature dependence of the reorganization energy comes from the variation of the refractive index with temperature.

This is easy to appreciate from the Marcus equation for the solvent reorganization energy, $\lambda_s(T) \propto c_0(T)$, in which λ_s is proportional to the Pekar factor $c_0(T) = \epsilon_\infty(T)^{-1} - \epsilon_s(T)^{-1}$. Here, the high-frequency dielectric constant $\epsilon_\infty(T) = n(T)^2$ is typically given in terms of the refractive index $n(T)$, and $\epsilon_s(T)$ is the static dielectric constant of the solvent. Both of them obviously change with temperature and the effects of $\epsilon_\infty(T)$ and $\epsilon_s(T)$ on $\lambda_s(T)$ are typically of the same order of magnitude.[23] This observation demands the use of polarizable force fields in numerical simulations, which can reproduce both $\epsilon_\infty(T)$ and $\epsilon_s(T)$. Such force fields are mostly unavailable even for the simplest solvents, and coarse-grained models based on experimental input are currently a better choice for the modeling.

Another alternative is to use dielectric continuum models, along with the numerical solution of the Poisson boundary value problem, to estimate the solvation free energies.[29,44] In this approach, temperature enters the Gibbs solvation energy through $\epsilon_s(T)$. In contrast, two dielectric constants, $\epsilon_\infty(T)$ and $\epsilon_s(T)$, are required for the calculation of $\lambda(T)$ given as the difference between the overall solvation free energy and the free energy of solvation by the fast electronic subsystem.[45] Such theoretical algorithms severely underestimate the dependence of the solvation free energy on temperature and thus produce too low values of the solvation entropy[16,17,26,46] (dashed lines in Figure 2). Not surprisingly, dielectric continuum calculations do not produce detectable maxima in the Arrhenius coordinates and are incapable of describing the experimental data reported here (Figure S4b in SI).

We have applied our theoretical algorithm coded into the software suite SolvMol[27,28] to model the temperature variation of λ_s and ΔG_s. The algorithm used for the calculations is based on coarse-graining the liquid into the pair correlation functions describing the orientational and density fluctuations in the bulk liquid.[27] Those are integrated in reciprocal $\mathbf{k}$-space with the spatial Fourier transforms of the electric field of the donor-acceptor complex to calculate the solvation free energies. The granularity of the solvent enters through the dependence of the distribution functions of the bulk liquid on the wavevector $\mathbf{k}$ (see Methods). Such a dependence physically describes correlated fluctuations in the solvent on different length-scales $\propto k^{-1}$.

Both λ_s and ΔG_0 are decaying functions with increasing temperature. However, λ_s is positive, while ΔG_0 is negative. The combination of λ_s becoming less positive and ΔG_0 becoming more negative at higher temperatures produces the point of equality at T^*, i.e., the crossing point between λ_s and the driving force $-\Delta G_0$, as shown in Figure 2. The temperature T^* defines the maximum rate, at which the activation barrier is zero, $G_a(T^*) = 0$ (Figure 1).

The calculations shown by the solid lines in Figure 4 were done by using the Bixon-Jortner formula[47] (eqs (7)–(8)) with the frequency of intramolecular vibrations $\omega_v = 1612$ cm^{-1} and the vibrational reorganization energy $\lambda_v = 0.14$ eV as calculated from DFT and CDFT (see Methods and SI). The calculated values of ω_v, λ_v, λ_s, and ΔG_s were used to produce the rates of both charge recombination (Figure 4a) and of two reactions of charge separation (Figure 4b). The electron-transfer matrix element V in eq (7) and the gas-phase energy ΔE_g in eq (5) were varied to produce the global fit of all experimental rates. The results of the fits are listed in Table 1. As is schematically depicted in Figure 1, the reaction is in the electron transfer inverted region at higher temperatures, switching to the normal regime after passing the maximum of activationless electron transfer at temperature T^*. Intramolecular vibrations affect the energy-gap law in the inverted region,[47] making the inverted parabola more shallow on its high-temperature wing. We have compared the Bixon-Jortner equation in the Arrhenius coordinates to the classical Marcus equation, ne-

glecting quantum intramolecular vibrations, in Figure S4a in SI. As is typically observed for the energy gap law in $\ln(k_{ET})$ vs $-\Delta G_0$ coordinates, the classical equation fails to reproduce the rates in the inverted region of electron transfer.

Our calculated $\lambda_s \simeq 0.87$ eV at $T = 297$ K (Figure 2) is close to the values reported in the literature based on the analysis of the Marcus energy gap law ($0.76-0.78$ eV for related dyads in tetrahydrofuran at 300 K[48]). As another test of consistency of calculations, we find that the sums of reaction free energies calculated for two charge-separation reactions and the recombination reaction, 1.85 (CS1) and 1.76 (CS2) eV, are very close in magnitude to optical excitation energies of, correspondingly, 1.91 and 1.75 eV[49] (Table 1). There is an overall good agreement between the theoretical model and experimental results.

Discussion

The vast majority of experimental tests of the Marcus theory and observation of the inverted region have used chemical alteration and the corresponding change of the driving force as the means to produce the bell-shaped curve. The experimental data and the theoretical analysis reported here offer a significant shift of focus to other environment parameters, temperature in this study. Miller and co-workers have recently employed pressure with the same goal and were able to continuously tune the reaction free energy by nearly 0.3 eV in nonpolar solvents to pass the maximum of the inverted parabola.[50] In an attempt to pass the maximum by varying temperature we find an anti-Arrhenius increase of rate with cooling at higher temperatures. This unusual behavior is followed, after passing the point of zero activation barrier, by the return to the commonly anticipated decay with further cooling. The very possibility of this unusual temperature law is related to a strong dependence of the activation free energy $G_a(T)$ on temperature in eq (2). We stress that this is a fundamentally important mechanistic property of electron transfer reactions in polar liquids, leading to the novel phenomena discussed in this article.

The ability to observe the rate maximum is a useful addition to the set of tools available for studies of mechanistic principles of electron transfer. Locating the maximum does not give direct access to the reaction free energy and the reorganization (free) energy, but fixes their sum (eq (1)). The results presented here speak to the need to incorporate temperature-dependent $\lambda_s(T)$ and $\Delta G_0(T)$ into the analysis of kinetic data. The results shown in Figure 2 suggest that the temperature dependence in the form $a + b/T$ provides a physically justified fitting function. Note that this temperature law directly follows from constant-volume microscopic theories of solvation separating the solvent response into orientational and density components.[22,23] The temperature dependence of solvation free energies at constant pressure is more complex because of thermal expansion, but the overall hyperbolic form is basically preserved for both $\lambda_s(T)$ and $\Delta G_0(T)$.

Although the temperature effect was demonstrated here only for a particular molecule carrying electron transfer, the theory shows that it is applicable to any system of molecules in solution. Whether or not a bell-shaped curve is found experimentally depends upon the details of molecule, solvent, and temperature range accessible.

Locating the rate maximum in the Arrhenius coordinates has certain advantages compared to the traditional approach of chemically modifying the donor-acceptor complex.[4,7,8,51] Chemical modification affects all mechanistic parameters of electron transfer, and not just driving force. Thus bell-shaped curves derived from such data actually represent many kinds of molecules, rather than one, each with its own value of V, etc. This complication is avoided when the bell-shaped law is accessed by varying thermodynamic variables such as temperature in this study or pressure in the study of Miller and co-workers.[50] The disadvantage of altering thermodynamic variables is that only a relatively narrow range of $G_a(T, P)$ can usually be sampled.

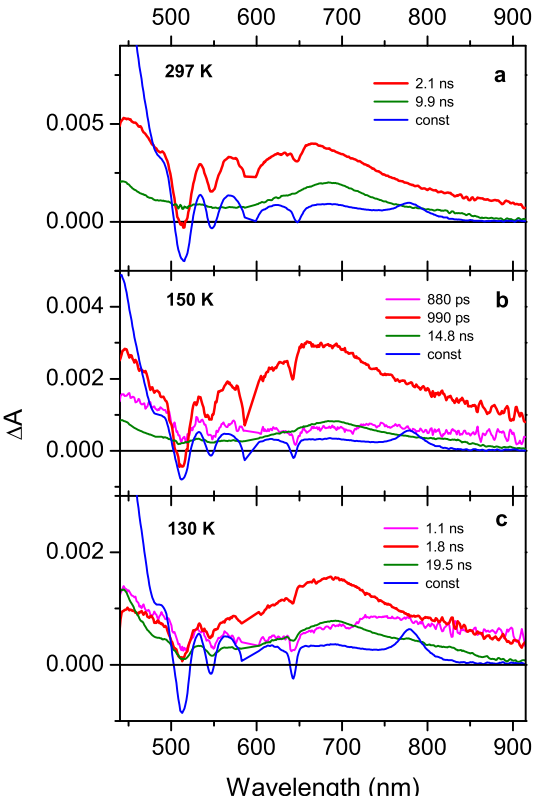

Figure 5: Transient absorption evolution-associated difference spectra extracted from the global analysis of data obtained with excitation at 590 nm in deaerated MTHF at different temperatures: 297 K (a), 150 K (b), and 130 K (c) (see SI for more detail). Transient absorption data were fitted with 3–4 exponential decay components. The lifetimes of formation of the charge separated state (magenta), obtained from the time-resolved fluorescence measurements, were fixed in the analysis. The rates of the charge recombination reaction shown in Figure 4a are extracted from the kinetic analysis.

Conclusions

A non-Arrhenius, bell-shaped temperature law was discovered for the reaction of charge recombination in a fullerene-porphyrin dyad. The physical origin of this phenomenon is a strong, approximately hyperbolic, variation of the solvation free energies entering the activation barrier of electron transfer with increasing temperature.

Methods

Theoretical calculations. The origin of the rate maximum and of the "inverted parabola" itself are now well understood. The Marcus energy gap law is a reflection of the Gaussian statistics of thermal bath fluctuations bringing the donor and acceptor energy levels into resonance.[52–54] Specifically, one assigns the energy difference between electronic levels of the acceptor and donor to the electron-transfer reaction coordinate X.[19,55] Since many molecules of the solvent interact with the electron, the distribution $P(X)$ is Gaussian according to the central-limit theorem

$$P(X) = \frac{1}{\sqrt{2\pi\sigma_X^2}} \exp\left[-\frac{(X-\langle X\rangle)^2}{2\sigma_X^2}\right] \qquad (6)$$

The traditional Marcus formulation of the electron transfer theory[56] gives $\langle X\rangle$ in this equation as the sum of ΔG_0 and λ, $\langle X\rangle = \lambda + \Delta G_0$, and $\sigma_X^2 = 2k_{\mathrm{B}}T\lambda$.

The point of $X = 0$ is the transition state when electron can tunnel through the barrier separating the donor and acceptor. The tunneling frequency $V/\hbar$ is specified by the electron-transfer matrix element V. The rate of nonadiabatic electron transfer is then given by the Golden-Rule expression

$$k_{\mathrm{ET}} = (2\pi/\hbar)V^2 P(0) \qquad (7)$$

where $P(0)$ is the probability of reaching the activated state with $X = 0$. It can be given by the Bixon-Jortner equation[47] accounting for multiple vibronic channels to achieve the activated state

$$P(0) = e^{-S}\sum_{n=0}^{\infty}\frac{S^n}{n!}P_n \qquad (8)$$

Here, $P_n = P(-n\hbar\omega_v)$ is the Gaussian probability

evaluated at $X = -n\hbar\omega_v$.

In eq (8), ω_v is the effective frequency representing quantum vibrations of the donor-acceptor complex and $S = \lambda_v/(\hbar\omega_v)$ is the Huang-Rhys factor involving the reorganization energy of quantum vibrations λ_v. Equation (8) is an approximate form of a more general expression for radiationless transition rates derived in the limit of quantum vibrations $\hbar\omega_v \gg k_B T$.[57] Therefore, the Marcus reorganization energy λ absorbs into itself all classical modes, both the solvent polarization and classical intramolecular vibrations.

The calculations of the rates shown in Figure 4 were done by using Eqs. (7) and (8) with the gas-phase parameters listed in Table 1. The vibrational reorganization energy was calculated as the difference of vertical transition energies in the initial and final electron-transfer states in vacuum (see SI).

The solvation calculations were done within the microscopic modeling of the solvent[27] realized in the program SolvMol.[28] The program uses experimental parameters of the solvent at a given temperature to calculate the polarization correlation functions required for the solvation calculations. The input solvent parameters include the effective molecular diameter $\sigma(T)$,[58] the dielectric constants $\epsilon_\infty(T)$ and $\epsilon_s(T)$, and the solvent density $\rho(T)$. Additional parameters required for calculating the dipolar response are the molecular gas-phase dipole μ and polarizability α. These parameters are used to calculate the condensed-phase dipole moment and polarizability by applying the Wertheim[59] mean-field theory of polarizable liquids. This procedure agrees exceptionally well with simulations of model polarizable solvents.[43] The data for $\epsilon_s(T)$ in MTHF are from Ref. 60. The detailed list of solvent parameters used in the calculations is given in SI.

Experimental procedures. Fluorescence and transient absorption decay kinetics of the $P - C_{60}$ dyad were measured with excitation to the one of porphyrins lower energy absorption bands (Q bands) at 590 nm. The solvent is Ar bubbled MTHF, and the temperature is varied from 120 K to 300 K (see apparatus description in SI). The fullerene moiety has a much weaker absorption at 590 nm. This rather featureless broad absorption band extends from UV to $\sim$ 705 nm. The porphyrin moiety shows a broad fluorescence band with maxima at about 650 and 720 nm. It overlaps well with the fullerene fluorescence (maxima at 710 and $\sim$ 800 nm). Therefore, both dyad moieties emit at 710 nm, at which frequency the decay kinetics were monitored. Fluorescence decay lifetimes were obtained by fitting the kinetics with 2 or 3 exponential decay components (Table S3 and Figure S6 in SI). The shortest lifetime is associated with the decay of porphyrin's singlet excited state and the longer lifetime is due to the decay of fullerene's singlet excited state (it was sometimes necessary to include a third decay component with the amplitude of $< 5\%$, which can be associated with minor impurities or fitting artifacts).

Rates of formation of the $P^{\cdot+} - C_{60}^{\cdot-}$ charge separated state from the porphyrin or fullerene singlet excited state were calculated as follows. The $^1P - C_{60}$ state decays in MTHF by photoinduced electron transfer to the fullerene, by singlet-singlet energy transfer to the fullerene, and by unimolecular photophysical processes of the porphyrin (fluorescence, internal conversion, and intersystem crossing). The overall rate constant combining these latter photophysical processes can be estimated as the reciprocal of the fluorescence lifetime of a model porphyrin ($\sim$ 10 ns). The rate constant for the energy transfer can be approximated by subtracting $(10\text{ ns})^{-1}$ from the reciprocal of fluorescence lifetime of $^1P - C_{60}$ in a nonpolar solvent such as cyclohexane (0.18 ns), where electron transfer does not occur. The electron transfer rate constant for formation of the $P^{\cdot+} - C_{60}^{\cdot-}$ charge separated state from $^1P - C_{60}$ can then be determined by subtraction of the two aforementioned rate constants, or $(0.18\text{ ns})^{-1}$, from the reciprocal of the first fluorescence decay lifetime of the dyad in MTHF. The rate constant for the formation of $P^{\cdot+} - C_{60}^{\cdot-}$ from $P - {}^1C_{60}$ can be determined similarly by subtracting the reciprocal of the fluorescence lifetime of a fullerene model compound $(1.3\text{ ns})^{-1}$ from the reciprocal of the second longer lifetime associated with $P - {}^1C_{60}$ in MTHF.

Transient absorption evolution-associated difference spectra (EADS) were obtained from global fitting of the kinetics with 3 or 4 exponential decay components (Table S4 and the data analysis in SI). Lifetimes of singlet excited states (associated EADS in magenta) obtained from time-resolved fluorescence measurements were fixed in the analysis. The EADS at 130 K, 150 K, and 297 K are shown in Figure 5. The 0.88 ns and 1.1 ns EADS (magenta lines) can be associated mostly with the decay of the $P - {}^1C_{60}$ excited state. They show a broad induced absorption and stimulated emission at 710 nm characteristic of fullerene. These spec-

tra are to some extent mixed with a much faster decaying singlet excited state of porphyrin formed during the excitation at 590 nm. They therefore show ground state bleaching due to the porphyrin Q bands around 510, 550, 590 and 650 nm. The 2.1 ns, 0.99 ns, and 1.8 ns EADS (red lines) display the same porphyrin Q-bands bleaching superimposed on a broad induced absorption at $\sim$ 680 nm characteristic of the porphyrin radical cation. They, therefore, can be associated with the decay of the $P^{\cdot+} - C_{60}^{\cdot-}$ charge separated state formed from the singlet excited states of the dyad (EADS in magenta lines). It decays to the ground state and, therefore, rate constants for charge recombination in the dyad at different temperatures (Figure 4a) can be calculated as reciprocal lifetimes associated with EADS shown by red lines. At 297 K, the formation of the charge-separated state is much faster than the instrument response and therefore it appears as an instantaneous process. The 9.9 ns, 14.8 ns and 19.5 ns EADS (green lines) show characteristic induced absorption at $\sim$ 700 nm associated with the $P - {}^3C_{60}$ excited state formed from the fullerene singlet excited state in competition with the charge separation. The 19.5 ns EADS (Figure 5c) is mixed with the porphyrin triplet excited state (see induced absorption at 450 nm and bleaching of Q bands) formed in parallel to charge separation from the slower decaying porphyrin singlet excited state at lower temperatures. The fullerene triplet excited state decays by triplet energy transfer to the porphyrin to give the porphyrin triplet excited state. The nondecaying (constant in the time window of the measurement) EADS (blue lines) show the porphyrin Q band bleaching and induced absorption at 780 nm and 450 nm characteristic of the $^3P - C_{60}$ excited state. This final excited state decays to the ground state in milliseconds.

Supporting Information Available: Calculation procedures, quantum calculations in vacuum, properties of the solvent, and additional experimental data and procedures. This material is available free of charge via the Internet at `http://pubs.acs.org/`.

Author Information:
Corresponding author: *`dmitrym@asu.edu`
Notes: The authors declare no competing financial interest.

Acknowledgement This research was supported by the Office of Basic Energy Sciences, Division of Chemical Sciences, Geosciences, and Energy Biosciences, Department of Energy (DE-FG02-03ER15393) and (DE-SC0015641, DVM). CPU time was provided by the National Science Foundation through XSEDE resources (TG-MCB080071).

References

(1) Marcus, R. A. *J. Chem. Phys.* **1965**, *43*, 679.

(2) Marcus, R. A.; Sutin, N. *Biochim. Biophys. Acta* **1985**, *811*, 265–322.

(3) Miller, J. R.; Calcaterra, L. T.; Closs, G. L. *J. Am. Chem. Soc.* **1984**, *106*, 3047–3049.

(4) Closs, G. L.; Miller, J. R. *Science* **1988**, *240*, 440–447.

(5) Barbara, P. F.; Meyer, T. J.; Ratner, M. A. *J. Phys. Chem.* **1996**, *100*, 13148–13168.

(6) Imahori, H.; Tamaki, K.; Guldi, D. M.; Luo, C.; Fujitsuka, M.; Ito, O.; Sakata, Y.; Fukuzumi, S. *J. Am. Chem. Soc.* **2001**, *123*, 2607–2617.

(7) Schuster, D. I.; Cheng, P.; Jarowski, P. D.; Guldi, D. M.; Luo, C.; Echegoyen, L.; Pyo, S.; Holzwarth, A. R.; Braslavsky, S. E.; Williams, R. M.; Klihm, G. *J. Am. Chem. Soc.* **2004**, *126*, 7257–7270.

(8) Guldi, D. M. *Phys. Chem. Chem. Phys.* **2007**, *9*, 1400.

(9) Tvrdy, K.; Frantsuzov, P. A.; Kamat, P. V. *Proc. Nat. Acad. Sci.* **2011**, *108*, 29–34.

(10) Olshansky, J. H.; Ding, T. X.; Lee, Y. V.; Leone, S. R.; Alivisatos, A. P. *J. Am. Chem. Soc.* **2015**, *137*, 15567–15575.

(11) Kuss-Petermann, M.; Wenger, O. S. *Angew. Chem. Int. Ed.* **2015**, *55*, 815–819.

(12) Kuss-Petermann, M.; Wenger, O. S. *J. Am. Chem. Soc.* **2016**, *138*, 1349–1358.

(13) Ohta, N.; Mikami, S.; Iwaki, Y.; Tsushima, M.; Imahori, H.; Tamaki, K.; Sakata, Y.; Fukuzumi, S. *Chem. Phys. Lett.* **2003**, *368*, 230–235.

(14) Angell, C. A. *Science* **1995**, *267*, 1924–1935.

(15) Born, M. *Z. Phys.* **1920**, *1*, 45–48.

(16) Roux, B.; Yu, H.-A.; Karplus, M. *J. Phys. Chem.* **1990**, *94*, 4683.

(17) Lynden-Bell, R. M.; Rasaiah, J. C. *J. Chem. Phys.* **1997**, *107*, 1981–1991.

(18) Vath, P.; Zimmt, M. B.; Matyushov, D. V.; Voth, G. A. *J. Phys. Chem. B* **1999**, *103*, 9130.

(19) Warshel, A. *J. Phys. Chem.* **1982**, *86*, 2218–2224.

(20) Matyushov, D. V.; Voth, G. A. *J. Chem. Phys.* **2000**, *113*, 5413.

(21) Blumberger, J.; Sprik, M. *Theor. Chem. Acc.* **2006**, *115*, 113–126.

(22) Matyushov, D. V. *Mol. Phys.* **1993**, *79*, 795.

(23) Matyushov, D. V. *Acc. Chem. Res.* **2007**, *40*, 294–301.

(24) Derr, D. L.; Elliott, C. M. *J. Phys. Chem. A* **1999**, *103*, 7888.

(25) Vath, P.; Zimmt, M. B. *J. Phys. Chem. A* **2000**, *104*, 2626.

(26) Ghorai, P. K.; Matyushov, D. V. *J. Phys. Chem. A* **2006**, *110*, 8857–8863.

(27) Matyushov, D. V. *J. Chem. Phys.* **2004**, *120*, 7532–7556.

(28) SolvMol Package, Copyright ASU. 2008; `http://theochemlab.asu.edu/?q=SolvMol`.

(29) Rocchia, W.; Sridharan, S.; Nicholls, A.; Alexov, E.; Chiabrera, A.; Honig, B. *J. Comp. Chem.* **2002**, *23*, 128–137.

(30) Heitele, H.; Finckh, P.; Weeren, S.; Pollinger, F.; Michel-Beyerle, M. E. *J. Phys. Chem.* **1989**, *93*, 5173–5179.

(31) Gust, D.; Moore, T. A.; Moore, A. L. *Acc. Chem. Res.* **1993**, *26*, 198.

(32) Gust, D.; Moore, T. A.; Moore, A. L. *Acc. Chem. Res.* **2009**, *42*, 1890–1898.

(33) Guldi, D. M.; Rahman, G. M. A.; Sgobba, V.; Ehli, C. *Chem. Soc. Rev.* **2006**, *35*, 471–487.

(34) Lee, S.-H.; Larsen, A. G.; Ohkubo, K.; Cai, Z.-L.; Reimers, J. R.; Fukuzumi, S.; Crossley, M. J. *Chem. Sci.* **2012**, *3*, 257–269.

(35) Fukuzumi, S.; Ohkubo, K.; Suenobu, T. *Acc. Chem. Res.* **2014**, *47*, 1455–1464.

(36) Kim, H. B.; Kitamura, N.; Kawanishi, Y.; Tazuke, S. *J. Am. Chem. Soc.* **1987**, *109*, 2506–2508.

(37) Davis, W. B.; Ratner, M. A.; Wasielewski, M. R. *J. Am. Chem. Soc.* **2001**, *123*, 7877.

(38) Newton, M. D. *Adv. Chem. Phys.* **1999**, *106*, 303.

(39) Gray, C. G.; Gubbins, K. E. *Theory of Molecular Liquids*; Clarendon Press: Oxford, 1984.

(40) Reynolds, L.; Gardecki, J. A.; Frankland, S. J. V.; Maroncelli, M. *J. Phys. Chem.* **1996**, *100*, 10337–10354.

(41) Perng, B.-C.; Newton, M. D.; Raineri, F. O.; Friedman, H. L. *J. Chem. Phys.* **1996**, *104*, 7153.

(42) Matyushov, D. V.; Voth, G. A. *J. Chem. Phys.* **1999**, *111*, 3630.

(43) Gupta, S.; Matyushov, D. V. *J. Phys. Chem. A* **2004**, *108*, 2087.

(44) Honig, B.; Sharp, K.; Yang, A. S. *J. Phys. Chem.* **1993**, *97*, 1101–1109.

(45) Sharp, K. A. *Biophys. J.* **1998**, *74*, 1241.

(46) Milischuk, A. A.; Matyushov, D. V.; Newton, M. D. *Chem. Phys.* **2006**, *324*, 172–194.

(47) Bixon, M.; Jortner, J. *Adv. Chem. Phys.* **1999**, *106*, 35.

(48) D'Souza, F.; Chitta, R.; Ohkubo, K.; Tasior, M.; Subbaiyan, N. K.; Zandler, M. E.; Rogacki, M. K.; Gryko, D. T.; Fukuzumi, S. *J. Am. Chem. Soc.* **2008**, *130*, 14263–14272.

(49) Kodis, G.; Liddell, P. A.; Moore, A. L.; Moore, T. A.; Gust, D. *J. Phys. Org. Chem.* **2004**, *17*, 724–734.

(50) Holroyd, R.; Miller, J. R.; Cook, A. R.; Nishikawa, M. *J. Phys. Chem. B* **2014**, *118*, 2164–2171.

(51) Imahori, H.; Yamada, H.; Guldi, D. M.; Endo, Y.; Shimomura, A.; Kundu, S.; Yamada, K.; Okada, T.; Sakata, Y.; Fukuzumi, S. *Angew. Chem. Int. Ed.* **2002**, *41*, 2344–2347.

(52) Kuharski, R. A.; Bader, J. S.; Chandler, D.; Sprik, M.; Klein, M. L.; Impey, R. W. *J. Chem. Phys.* **1988**, *89*, 3248–3257.

(53) Zhou, H.-X.; Szabo, A. *J. Chem. Phys.* **1995**, *103*, 3481.

(54) Bader, J. S.; Cortis, C. M.; Berne, B. J. *J. Chem. Phys.* **1997**, *106*, 2372–2387.

(55) Zusman, L. D. *Chem. Phys.* **1980**, *49*, 295–304.

(56) Marcus, R. A. *Annu. Rev. Phys. Chem.* **1964**, *15*, 155–196.

(57) Kestner, N. R.; Logan, J.; Jortner, J. *J. Phys. Chem.* **1974**, *78*, 2148–2166.

(58) Schmid, R.; Matyushov, D. V. *J. Phys. Chem.* **1995**, *99*, 2393.

(59) Wertheim, M. S. *Mol. Phys.* **1979**, *37*, 83–94.

(60) Streck, C.; Richert, R. *Ber. Bunsenges. Phys. Chem.* **1994**, *98*, 619–625.

Figure Legends

Figure 1 The bell-shaped (Marcus) energy gap law vs the reaction driving force $-\Delta G_0$ (a) and the bell-shaped law vs $1/T$ (Arrhenius coordinates, b). In both cases, the top of the inverted parabola corresponds to zero activation free energy, $G_a = 0$. "N" and "I" indicate, correspondingly, the normal and inverted regions of electron transfer

Figure 2 Temperature variation of the solvent reorganization energy $\lambda_s(T)$ (red solid line) and the driving force $-\Delta G_0$ (black solid line) calculated for the charge recombination reaction in 2-methyltetrahydrofuran (MTFH). The left axis refers to the results of the microscopic solvation model SolvMol,[27,28] while the right axis and the dashed lines refer to λ_s (red) and ΔG_s (blue) calculated in the dielectric continuum model of the solvent by using the software package DelPhi.[29] The vertical arrow indicates the temperature T^* at which zero activation barrier, $G_a = 0$, is reached in the SolvMol calculations (eq (1) and Figure 1)

Figure 3 Structure of the porphyrin-fullerene dyad

Figure 4 Rate constant in Arrhenius coordinates for charge recombination ($k_R(T)$, a) and charge separation ($k_{CS1}(T)$ and $k_{CS2}(T)$, b) in MTHF. The points represent experimental data and the solid lines refer to the theoretical calculations with the SolvMol package.[27,28] The experimental errors for CR in (a) are within 5% and for CS in (b) within 10%. The error bars in (b) are not shown since they are nearly the size of the points. All theoretical calculations were done with a single set of parameters listed in Table 1 (fitting parameters V and ΔE_g and calculated λ_v; experimental parameters of the solvent are used for the solvation calculations)

Figure 5 Transient absorption evolution-associated difference spectra extracted from the global analysis of data obtained with excitation at 590 nm in deaerated MTHF at different temperatures: 297 K (a), 150 K (b), and 130 K (c) (see SI for more detail). Transient absorption data were fitted with 3–4 exponential decay components. The lifetimes of formation of the charge separated state (magenta), obtained from the time-resolved fluorescence measurements, were fixed in the analysis

Table 1: Parameters of electron transfer reactions (eV).

	Gas			Solvent[a]		Total[b]		
Reaction	$V \times 10^3$	λ_v	ΔE_g	λ_s	ΔG_s	ΔG_0	$\Delta E_{\rm abs}$[c]	$h\nu_{\rm abs}$[d]
R	0.25	0.14	−2.18[e]	1.15	1.0	−1.18		
CS1	2.5	0.14	0.33	1.15	−1.0	−0.67	1.85	1.91
CS2	2.8	0.14	0.42	1.15	−1.0	−0.58	1.76	1.75

[a] λ_s and ΔG_s are given at the temperature T^* of the maximum: $\lambda_s(T^*) + \Delta G_0(T^*) = 0$, $T^* \simeq 150$ K.
[b] Calculated at 300 K. [c] Calculated as $\Delta E_{\rm abs} = -\Delta G_0^{\rm CS} - \Delta G_0^{\rm CR}$ for two CS reactions, Eq. (4).
[d] Experimental absorption energies producing photoexcited P* (CS1) and C_{60}^* (CS2) states.
[e] $\Delta E_g = -3.0$ eV was calculated with DFT, see Table S1 in SI.

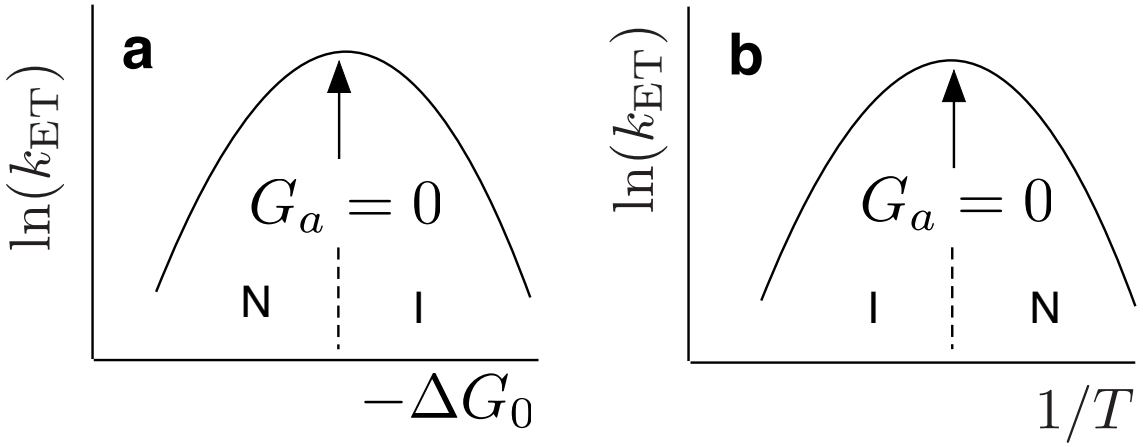

Figure 1

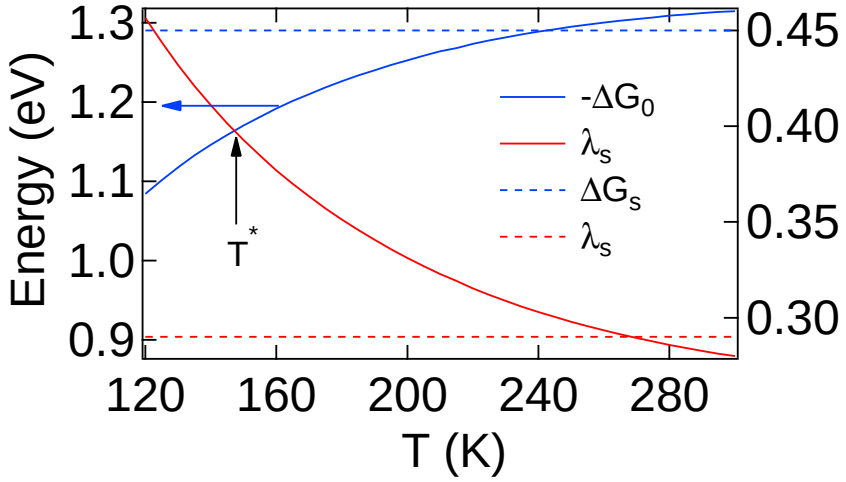

Figure 2

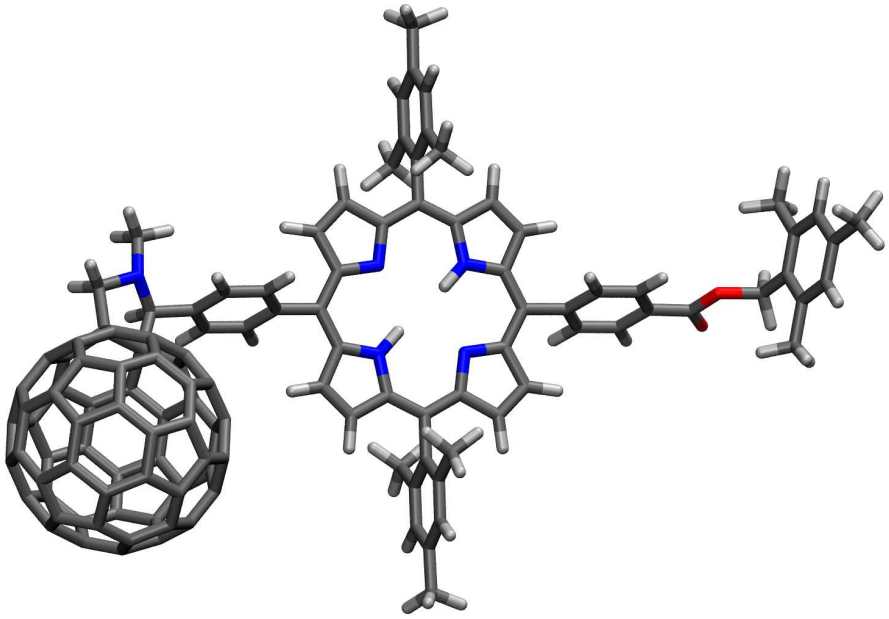

Figure 3

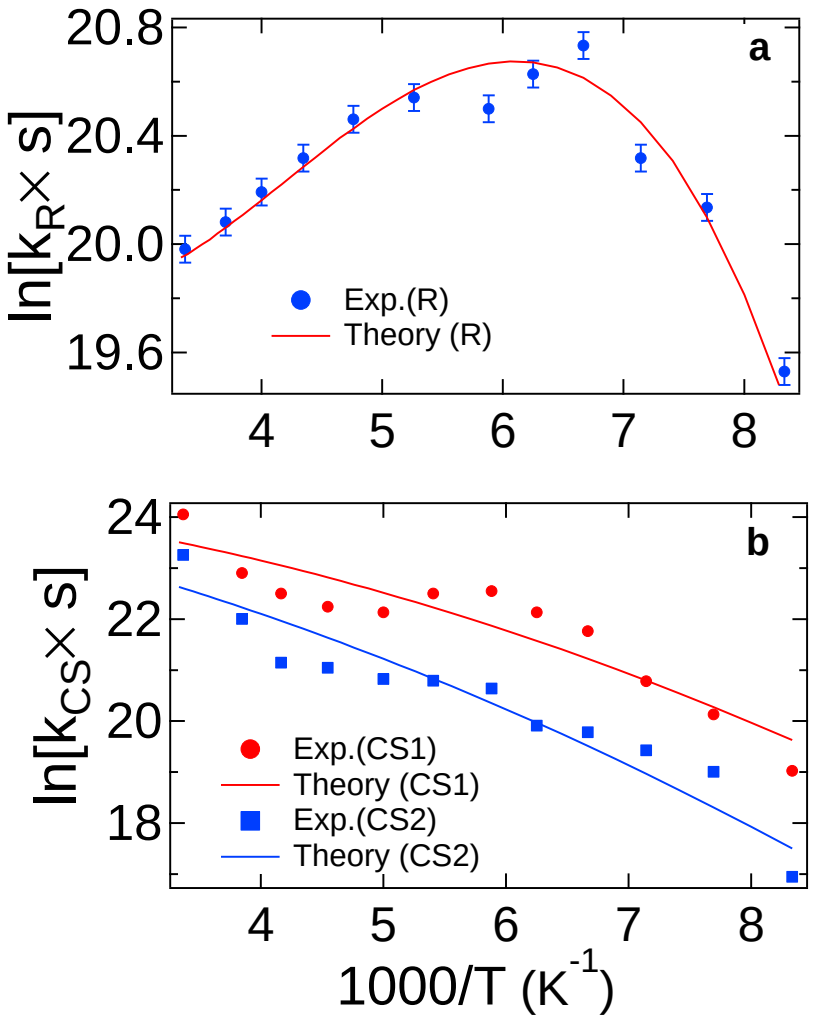

Figure 4

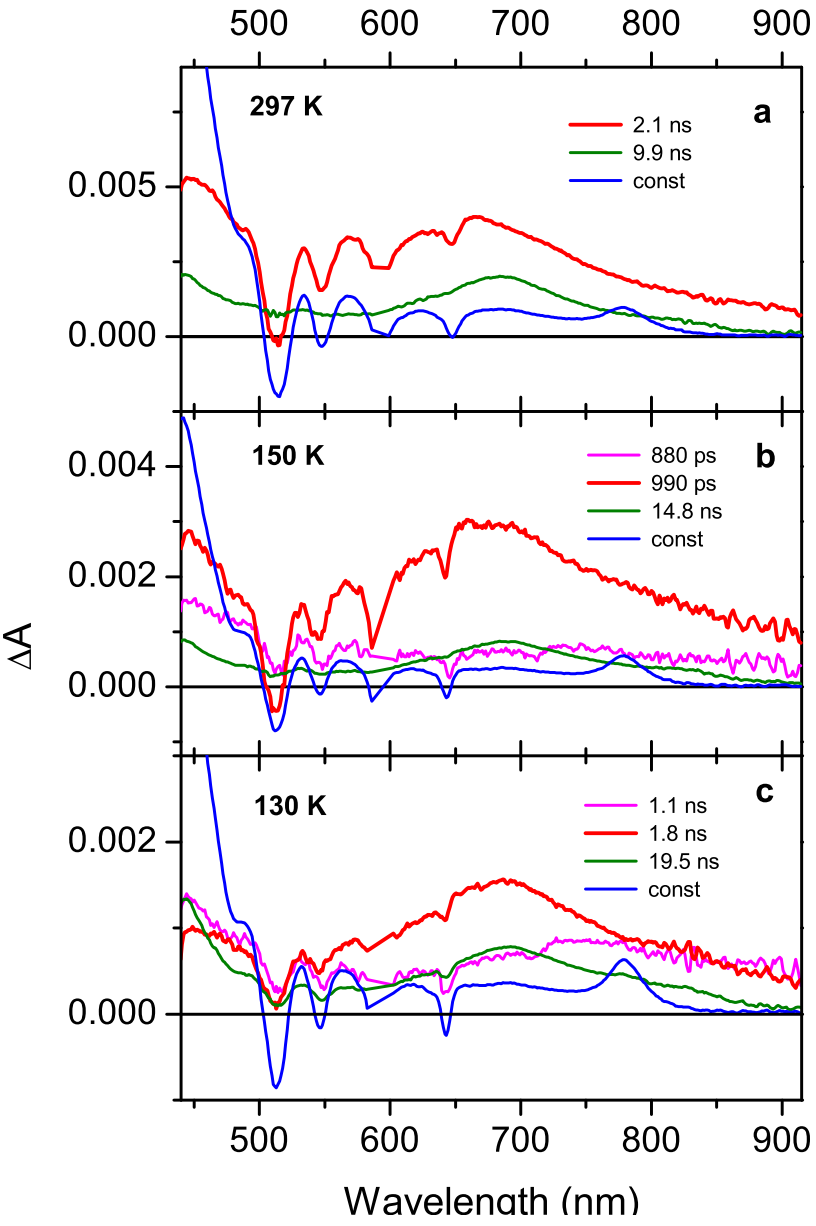
297 K
a
2.1 ns
9.9 ns
const
150 K
b
880 ps
990 ps
14.8 ns
const
130 K
c
1.1 ns
1.8 ns
19.5 ns
const
ΔA
0.005
0.000
0.004
0.002
0.000
0.002
0.000
500
600
700
800
900
Wavelength (nm)

Figure 5

Graphical TOC Entry